Single-Dish Radio Astronomy: Techniques and Applications
ASP Conference Series, Vol. 278, 2002
S. Stanimirović, D. R. Altschuler, P. F. Goldsmith, and C. J. Salter

Pulsar Observations I. – Propagation Effects, Searching, Distance Estimates, Scintillations and VLBI

James M. Cordes
Astronomy Department, Cornell University, Ithaca, New York 14850, USA

Abstract. Propagation effects from the interstellar medium (ISM) are discussed along with their implications for pulsar observations and analysis. Then I discuss (1) dedispersion techniques, particularly that for postdetection systems; (2) pulsar search analysis and the role of instrumental, interstellar and orbital broadening of pulses; and (3) methods for determining distances to pulsars and a new Galactic electron density model now nearly completed. I end by discussing new observations including multibeam searches and VLBI astrometric observations.

1. Introduction

Radio pulsar signals consist of pulsed continuum noise that can be highly elliptically polarized. The signals have a very high degree of spatial coherence but very little temporal coherence. Pulses are modified significantly as they propagate through the ionized and magnetized interstellar medium. The signal complexity requires refined techniques for discovering new pulsars and for extracting all information contained in pulsar signals.

In this article, I discuss the phenomenology and measurement of pulsar signals. Methodology will center on 'postdetection' methods, i.e. those that involve recording the signal after it has been squared. Predetection methods are discussed by I. Stairs in a separate lecture.

2. Wave Propagation Basics

For the interstellar medium (ISM), the plasma frequency is $\nu_p \approx 1.56\,\mathrm{kHz}\,(n_e/0.03\,\mathrm{cm}^{-3})^{1/2}$ and the gyrofrequency is $\nu_\mathrm{B} \approx 2.8\,\mathrm{Hz} B_{\mu G}$. Magnetic fields introduce birefringence that is most easily detected as Faraday rotation. The index of refraction in a cold magnetized plasma like the ISM for $\nu \gg \nu_p$ and $\nu \gg \nu_{\mathrm{B}||}$ is (e.g. Thomson, Moran, & Swenson 2001)

$$n_{l,r} \approx 1 - {\nu_p}^2/2\nu^2 \mp {\nu_p}^2\nu_{\mathrm{B}||}/2\nu^3, \qquad (1)$$

where $\nu_p = (n_e e^2/\pi m_e)^{1/2}$ is the plasma frequency and $\nu_{\mathrm{B}||} = eB\cos\theta/m_e c$ is the electron gyrofrequency calculated for the magnetic field component along the line of sight; the $\mp$ cases apply for LHCP and RHCP waves.

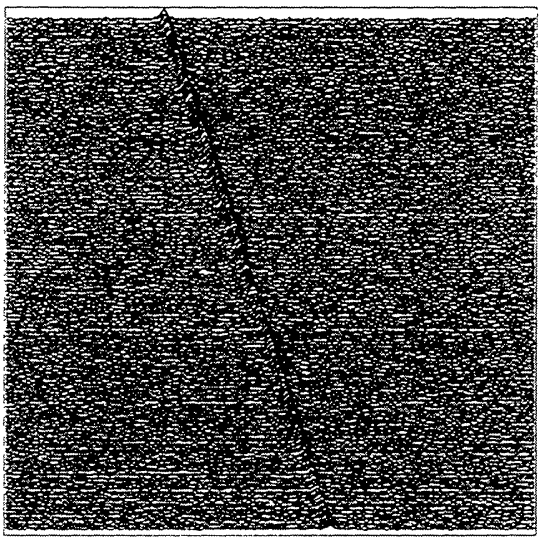

Figure 1. Frequency-pulse phase plot for PSR B1534+12 for 1024 frequency channels (vertical axis) at 0.43 GHz (Courtesy M. McLaughlin).

Dispersive arrival times & Faraday Rotation: The frequency dependent time delay (see Figure 1) is calculated by integrating (group velocity)$^{-1}$ = $dk/d\omega = c^{-1}\,(n_{l,r} + \nu dn_{l,r}/d\nu)$ along the line of sight, giving

$$t = t_{\rm DM} \pm t_{\rm RM}. \tag{2}$$

The dispersive time delay and the small correction due to birefringence are

$$t_{\rm DM} = \frac{e^2}{2\pi m_e c}\frac{\int_0^D ds\, n_e}{\nu^2} = 4.15\,{\rm ms}\ {\rm DM}\ \nu_{\rm GHz}^{-2}, \tag{3}$$

$$t_{\rm RM} = 2{\rm RM}c^2\nu^{-3} = 0.18\,{\rm ns}\ {\rm RM}\,\nu_{\rm GHz}^{-3}, \tag{4}$$

where the dispersion and rotation measures and their standard units (for D in pc, n_e in cm^{-3}, and $B_{||}$ in μG) are

$${\rm DM} = \int_0^D ds\, n_e(s) \quad ({\rm pc\,cm^{-3}}), \tag{5}$$

$${\rm RM} = \frac{e^3}{2\pi m_e^2 c^4}\int_0^D ds\, n_e B_{||} = 0.81\int_0^D ds\, n_e B_{||} \quad ({\rm rad\,m^{-2}}). \tag{6}$$

The birefringent delay is too small to be measureable in practical situations but is manifested as Faraday rotation of the plane of polarization. The differential phase between LHCP and RHCP is

$$\Delta\phi = \frac{2\pi}{\lambda}\int_0^D ds\,(n_r - n_l) = 2{\rm RM}\lambda^2, \tag{7}$$

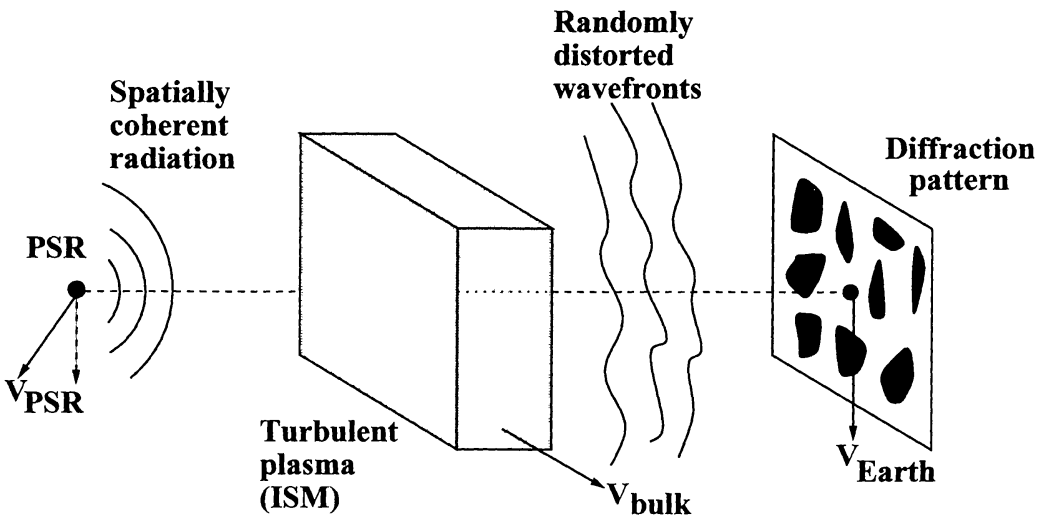

Figure 2. Geometry of scattering in the ISM that is responsible for a variety of seeing and scintillation effects.

where the factor of 2 accounts for the fact that the polarization position angle rotates over π when the phase rotates 2π.

Multipath Propagation: Interstellar Scattering & Scintillations: Phase perturbations from electron-density fluctuations are

$$\phi(\mathbf{x}_\perp, z) = \frac{2\pi}{\lambda}\int_0^D ds\, n_{l,r} \approx -\lambda r_e \int_0^D dz\, \delta n_e(\mathbf{x}_\perp, z), \tag{8}$$

where the classical electron radius is $r_e = e^2/m_e c^2$. Geometrical optics (see Figure 2) gives the *refraction angle*, $\theta_r = k^{-1}\nabla_\perp \phi$, while physical optics gives the *diffraction angle*, $\theta_d \sim \lambda/\ell_\perp$, where $\ell_\perp$ is the length scale on which the phase changes by ~ 1 radian. For the ISM, θ_d ranges from < 1 mas to ~ 1 arc sec at 1 GHz for different lines of sight.

Effects from multipath propagation include (Rickett 1990; Cordes & Lazio 1991):

Angular broadening ("seeing"): Compact radio sources of many kinds, Galactic and extragalactic, show angular broadening by amounts ranging from $\lesssim$1 mas to 1 arcsec at 1 GHz, depending on the distance and direction. The angular smearing scales approximately as ν^{-2}.

Time of arrival fluctuations: Changes in geometry induce DM variations. Also, variable scattering causes variable arrival times.

Pulse broadening: Multipath propagation causes a multiplicity of arrival times, usually seen as an exponential-like 'tail' to pulses from pulsars.

Diffractive intensity scintillations (DISS): Intensity variations in time and frequency on times scales $\sim$ 100 sec and frequency scales $\sim$ 1 MHz. These

scales are very highly dependent on frequency, direction and source distance and velocity. These variations result from diffraction of radiation into an angle $\theta_d \sim \lambda/\ell_d$, where ℓ_d is the diffraction scale, the transverse length on which the phase perturbation from δn_e is one radian.

Refractive intensity scintillation (RISS): Intensity variations from large scale focusing and defocusing of the radiation. The refraction scale is $\ell_r \sim D\theta_d$, implying the well known relation, $\ell_r \ell_d \sim \lambda D \sim$ (Fresnel scale)^2.

Spectral Broadening: Broadening of narrow spectral lines from a combination of scattering and time-variable geometry. The effect is very small in the ISM ($\lesssim$1 Hz) but has been measured from spacecraft viewed through the interplanetary medium.

Superresolution phenomena: The optical/atmospheric "Stars twinkle but planets do not" translates into "Pulsars twinkle, AGNs do not," at least for DISS. The (angular) isoplanatic scale for DISS is typically $\sim \ell_d/D \lesssim 10^{-6}$ arc sec at 1 GHz, or about $\times 10^3$ smaller than an AGN and $\times 10$ larger than a typical pulsar magnetosphere. Thus, we expect pulsars to show fully modulated scintillations in the strong scattering regime, whereas AGNs will not show DISS, typically. RISS is more forgiving of a large source size because it is caused by much larger turbulence scales than is DISS, with a critical angle $\sim \ell_r/D \sim \theta_d$. Thus, AGNs and masers, as well as pulsars, show RISS.

Scaling Laws for Pulse Broadening: Pulse broadening from multipath propagation is approximately

$$\tau_d \sim \frac{D\theta_d^2}{2c}. \tag{9}$$

The scaling laws are approximately $\theta_d \propto \nu^{-2}$ and $\tau_d \propto \nu^{-4}$. Figure 3 shows a strongly-scattered pulse at three frequencies for a large-DM pulsar compared to a low-DM pulsar with negligible scattering.

Pulse broadening is correlated with DM, though not perfectly. Figure 4 shows τ_d at 1 GHz plotted against DM along with a parabolic fit (solid line) and $\pm 1.5\sigma$ lines (dashed). The fit is with $\log DM$ as the independent variable:

$$\log \tau_d(\mu s) = -3.59 + 0.129 \log \mathrm{DM} + 1.02(\log \mathrm{DM})^2 - 4.4 \log \nu_{\mathrm{GHz}}. \tag{10}$$

The scattering time for individual pulsars can deviate considerably from the fit, with $\sigma_{\log \tau} = 0.65$.

Scintillations: Figure 5 shows diffractive interstellar scintillation (DISS) as a dynamic spectrum $I(t,\nu)$ and the 2D autocorrelation function (ACF) of the dynamic spectrum, $\langle I(t,\nu) I(t+\delta t, \nu+\delta\nu)\rangle$ with time and frequency lags $\delta t, \delta\nu$, and where angular brackets denote time average. Slices along the ACF axes have features whose widths yield the characteristic scintillation (or diffraction) bandwidth of $\Delta\nu_{\mathrm{d}}$ and time scale Δt_{d} of the DISS. Quoted values in the literature

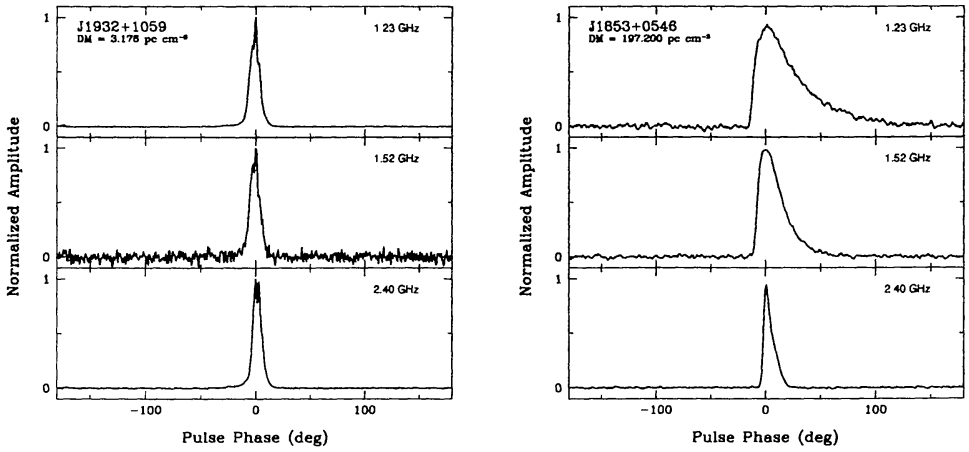

Figure 3. Left: Pulse shape at 3 frequencies for PSR J1932+1059 (aka B1929+10), a low DM pulsar whose profile evolution with frequency is all intrinsic. The low S/N at the middle frequency is due to DISS. Right: Pulse shape at 3 frequencies for PSR J1853+0546 showing the asymmetry caused by multipath propagation; the pulse-broadening time scales strongly with frequency, $\tau_d \propto \nu^{-4}$. Data are from R. Bhat et al. (unpublished).

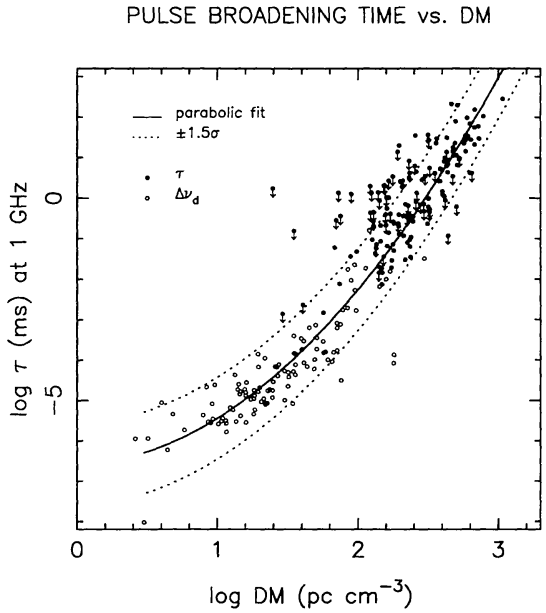

Figure 4. Pulse broadening time at 1 GHz plotted against dispersion measure. Filled circles indicate direct measurement of the scattering time; open circles represent scattering times estimated from scintillation bandwidth measurements. All measurements are scaled to 1 GHz using $\tau \propto \nu^{-4.4}$. The solid line is the parabolic fit given in Equation 10; dashed lines are at $\pm 1.5\sigma$.

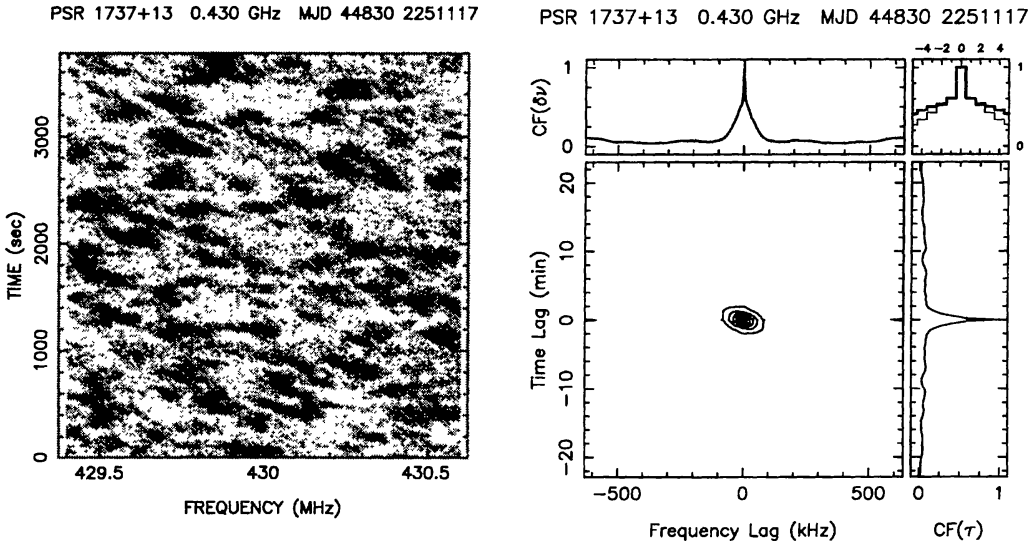

Figure 5. Left: Dynamic spectrum. Right: Autocorrelation function of the dynamic spectrum.

are usually taken to the halfwidth at half maximum for $\Delta\nu_{\rm d}$ and the halfwidth at 1/e for $\Delta t_{\rm d}$. These widths are strong functions of the strength of scattering. Scattering increases with wavelength and distance and is also much stronger in the inner Galaxy. For stronger scattering, the characteristic scales of the DISS get *smaller.*

DISS is important because it strongly modulates the pulsar intensity according to an *exponential* probability density function (PDF). For the more weakly scattered pulsars, an entire observation (i.e. the total bandwidth and duration) may comprise only one patch of constructive or destructive interference. Thus in a pulsar search, it is possible that a given object will be scintillated up or down. The exponential shape of the PDF implies that it is more likely to be scintillated downward. Therefore searches may profitably cover a given sky position more than once.

Scaling Laws from the Electron Density Wavenumber Spectrum: Electron-density variations are commonly described by a power-law wavenumber spectrum of the form (e.g. Armstrong, Rickett, & Spangler 1995)

$$P_{\delta n_e}(q) = C_n^2 q^{-\alpha}, \quad \frac{2\pi}{\ell_0} \le q \le \frac{2\pi}{\ell_1}, \tag{11}$$

where C_n^2 is the spectral coefficient of the wavenumber spectrum of δn_e, ℓ_1, ℓ_0 are the inner and outer scales of the turbulence and the spectrum vanishes outside the specified interval. Equation 11 explicitly assumes isotropic irregularities. Evidence for anisotropies exists but it is not clear on what length scale these are present. Also, there is strong evidence (from refractive effects) that the spectrum departs from a power law on scales $\sim 1 - 10$ AU. The spectral coefficient varies by many orders of magnitude between lines of sight, as diagnosed from scattering and scintillation observations.

The *scattering measure* is defined as (e.g. Cordes et al. 1991)

$$\mathrm{SM} = \int_0^D ds\, C_n^2(s). \tag{12}$$

Observables yield different effective values for SM because of different weight factors:

(1) $\mathrm{SM}_{\theta,x} = \mathrm{SM}$ for measurements of angular diameters of extragalactic sources;

(2) $\mathrm{SM}_{\theta,g} = 3\int ds\,(1-s/D)^2 C_n^2$ for angular diameters of galactic sources;

(3) $\mathrm{SM}_{\tau} = 6\int ds\,(s/D)(1-s/D) C_n^2$ for pulse broadening and scintillation measurements.

Units are usually $\mathrm{m}^{-20/3}$ for C_n^2 and kpc $\mathrm{m}^{-20/3}$ for SM. With ν in GHz, the seeing disk size (FWHM) is

$$\theta_d = \nu^{-11/5} \times \begin{cases} 128\,\mathrm{mas}\,\mathrm{SM}_{\theta,x}^{5/3} & \text{Extragalactic Sources} \\ 71\,\mathrm{mas}\,\mathrm{SM}_{\theta,g}^{5/3} & \text{Galactic Sources.} \end{cases} \tag{13}$$

For pulse broadening and scintillation bandwidth,

$$\tau_d = 0.90\,\mathrm{ms}\ \mathrm{SM}_{\tau}^{6/5}\nu^{-22/5}D, \tag{14}$$

$$\Delta\nu_{\mathrm{d}} = 0.171\,\mathrm{MHz}\ \mathrm{SM}_{\tau}^{-6/5}\nu^{22/5}(C_1/1.16)D^{-1}, \tag{15}$$

where D is in kpc and $C_1 = 1.16$ for a Kolmogorov spectrum. The DISS time scale is determined by the pulsar's transverse speed $V_{p\perp}$:

$$\Delta t_{\mathrm{d}} = 2.53\times 10^4\ \mathrm{km\ s^{-1}}\, W_{\mathrm{C}} W_{\mathrm{D,PM}} \frac{\sqrt{D\Delta\nu_{\mathrm{d}}}}{\nu V_{p\perp}}, \tag{16}$$

where W_{C} and $W_{\mathrm{D,PM}}$ are correction factors equal to unity for a uniform, Kolmogorov medium. See Cordes & Rickett (1998) for further discussion about W_{C}. The factor $W_{\mathrm{D,PM}}$ takes into account the spatial distribution of scattering material and is approximately

$$W_{\mathrm{D,PM}}(D) \approx \left[\frac{\mathrm{SM}_{\tau}}{3\mathrm{SM} - (\mathrm{SM}_{\theta,g} + \mathrm{SM}_{\tau})}\right]^{1/2}. \tag{17}$$

3. Dedispersion Techniques

Dispersion may be viewed as a delay of a pulse or as a phase rotation of its Fourier components. Correction for dispersion is done in two primary ways (e.g. Hankins & Rickett 1975). *Post-detection* schemes make use of a multichannel receiver, realized as an analog filter bank in the old days, or today as either an FFT

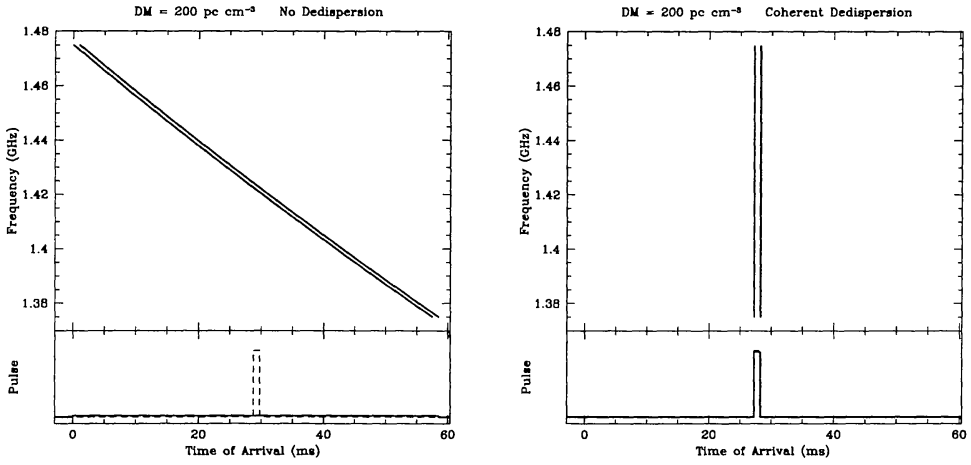

Figure 6. Schematic diagrams showing dispersive arrival times and postdetection dedispersion. Left: the top panel shows arrival time vs. frequency for a 1-ms wide pulse; the bottom panel shows the intrinsic pulse shape (dashed line) and the dispersed pulse (heavy line). Right: Coherent dedispersion corrects Fourier phases perfectly, yielding time resolution equal to the reciprocal of the total bandwidth.

system or correlation spectrometer. The detected (i.e. squared) outputs of each channel can be advanced to compensate for the delays from the dispersion law of Equation 3. *Predetection* methods correct the Fourier phases and are described further by I. Stairs. Post-detection devices achieve high-time resolution at high frequencies, but are limited by filter response times and by scattering at low frequencies. Predetection techniques use wider filters, so the filter response time can be much smaller than for the postdetection case. However, predetection methods are still limited by scattering at low frequencies and for large DM.

Figures 6-7 show the dispersion effect and its compensation in pre-and-post detection schemes schematically.

Minimum time resolution for postdetection Systems: The time resolution is determined by a combination of *dispersion over an individual channel* (with DM in pc cm^{-3}):

$$\Delta t_{\rm DM}(\Delta\nu) = 8.3\,\mu s\, DM\, \Delta\nu_{\rm MHz}\nu_{\rm GHz}^{-3}, \tag{18}$$

which is the differential form of Equation 3, and from the *impulse response* of an individual channel:

$$\Delta t_{\Delta\nu} \sim (\Delta\nu)^{-1} = 1\,\mu s(\Delta\nu_{\rm MHz})^{-1}. \tag{19}$$

For given DM and ν, the minimum dispersion time implied by Equations 18, 19 is

$$\Delta t_{DM,min}(\mu s) = \left(\frac{8.3DM}{\nu_{GHz}^3}\right)^{1/2}. \tag{20}$$

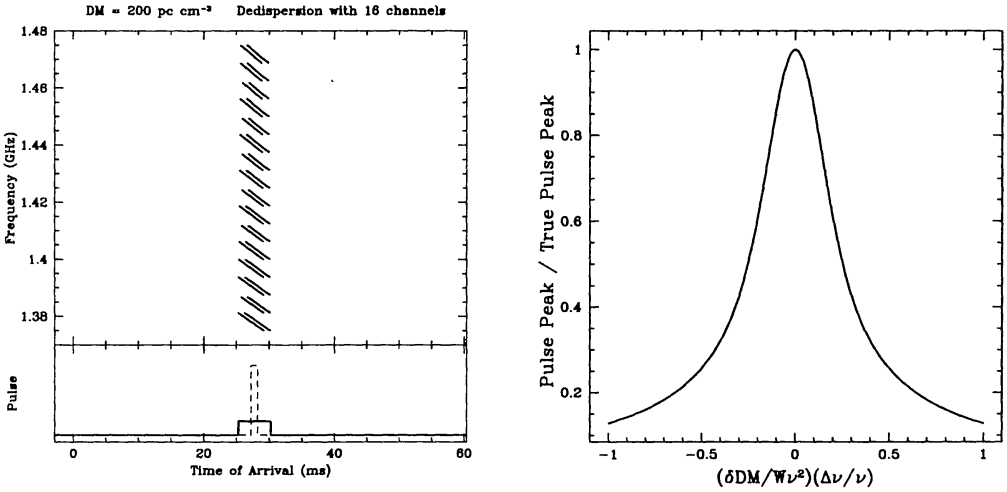

Figure 7. Left: the top panel shows how postdetection dispersion compensation yields residual dispersion across individual channels; the bottom panel shows that in this case the pulse is still significantly smeared. Smaller channel bandwidths yield less residual smearing but only to the limit where the dispersion smearing equals the impulse response time of the channel $\sim \Delta\nu_{\rm ch}^{-1}$. Right: Pulse amplitude loss from imperfect dedispersion using a DM in an error by δDM. The abcissa is the composite quantity $(\delta DM/W\nu^2)(\Delta\nu/\nu)$ with δDM in pc cm^{-3}, pulse width W in ms, and frequency ν and bandwidth $\Delta\nu$ in GHz. The width of the function ~ 0.52 (FWHM).

The minimum resolution due to the combined effects of dispersion and the filter response, which are equal, is $\sqrt{2}\Delta t_{DM,min}$. (The achievable resolution, of course, may be determined by scattering rather than dispersion)

How accurately must DM be known? To dedisperse optimally, DM must be known to a precision that is frequency, bandwidth and pulse-width dependent. For a Gaussian shaped pulse, the amplitude of the dedispersed pulse (relative to perfect dedispersion) for an error δDM is

$$I_{\rm max}(\delta{\rm DM}) = \frac{\sqrt{\pi}}{2}\zeta^{-1}{\rm erf}\,\zeta, \qquad \zeta = \frac{6.91\,{\rm ms}}{W}\frac{\delta{\rm DM}}{\nu^2}\frac{\Delta\nu}{\nu}, \tag{21}$$

where W is the intrinsic pulse width (FWHM) in ms and the units are pc cm^{-3}, GHz and GHz for δDM, ν and $\Delta\nu$, respectively. $I_{\rm max}$ is plotted in Figure 7 (right panel). The FWHM of the curve implies a DM tolerance

$$\delta{\rm DM} \approx 0.52\,{\rm pc\,cm^{-3}}\,\frac{W\nu^3}{\Delta\nu}. \tag{22}$$

Achievable Time Resolution vs. DM & Frequency: For postdetection systems the achievable time resolution is approximately the root-quadratic sum of the filter-response, dispersion smearing and pulse-broadening times:

$$\Delta t_{\rm min} = \left[(\Delta t_{DM})^2 + (\Delta t_{\Delta\nu})^2 + \tau_d^2\right]_{\rm min}^{1/2} = \left[2(\Delta t_{DM})^2 + (\tau_d)^2\right]^{1/2}. \tag{23}$$

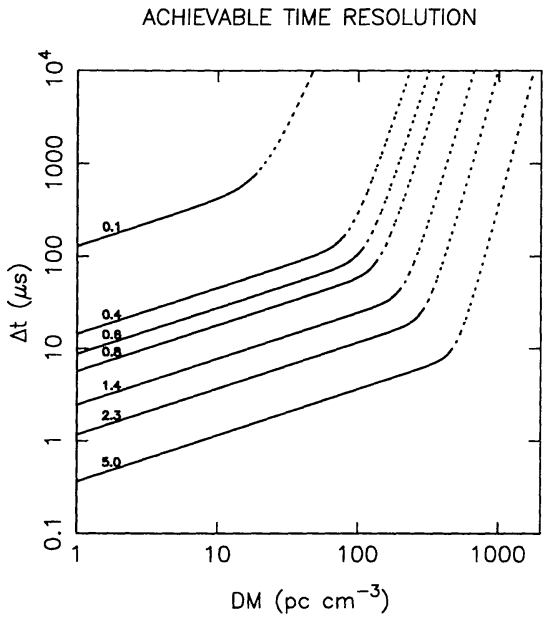

Figure 8. Best achievable time resolution of postdetection systems plotted against pulsar dispersion measure. The curves are labeled with radio frequency ranging from 0.1 to 5 GHz. (Solid lines) Time resolution is limited by dispersion; (Dashed lines) Time resolution limited by interstellar scattering. Note that predetection systems can achieve better time resolution than the post detection case if the latter is dispersion bound. But predetection systems will be limited by scattering according to the dashed curves shown here.

Figure 8 shows the minimum resolution plotted against DM for frequencies ranging from 0.1 to 5 GHz. The solid lines designate those DM-ν combinations that are *dispersion limited* while the dashed lines correspond to *scattering dominated* situations. Predetection dispersion removal over a bandwidth $B > (\Delta t)^{-1}$ can do better than postdetection schemes only if the latter are dispersion limited; that is, only for cases in Figure 8 where solid lines are plotted.

Viewed another way, there is a maximum DM for which some desired time resolution Δt can be achieved. Excluding scattering, the maximum DM is

$$\mathrm{DM}_{\mathrm{max},\Delta\nu} = \frac{(\Delta t_{\mu s})^2 \nu^3_{\mathrm{GHz}}}{16.6} \,. \tag{24}$$

However, at low frequencies scattering will limit even further the range of dispersion measures over which the specified time resolution can be obtained to a maximum:

$$\mathrm{DM}_{\mathrm{max,scatt}} = 0.86\,\mathrm{pc\ cm^{-3}} 10^{1.88(1+0.28\log \Delta t_{\mu s} + 1.22 \log \nu_{\mathrm{GHz}})^{1/2}} . \tag{25}$$

4. Post-Detection Pulsar Observations

Table 1 summarizes typical observations that are made with postdetection systems. The data rate that is output from the filterbanks or correlator systems before any processing (such as realtime or offline 'folding' of data according to a pulsar emphemeris) is typically 1-20 Mbytes s^{-1}.

Table 1. Post-Detection Observations & Parameters

Type	Δt (μs)	T (s)	N_ν	Comments
Searching	~ 100	$\gtrsim 100$	256 to 1024	polarizations summed Trial DMs: ~ 50 to 500 (ℓ, b) FFTs of length M Megasamples
Timing	10^{-3}P	~ 100	~ 256	polarizations summed (calibrated!)
Polarization	10^{-3}P	~ 100	~ 256	full Stokes
ISS	10^{-2}P	~ 3600	~ 1024	polarizations summed
Single Pulse	10^{-3}P	~ 3600	$\gtrsim 256$	full Stokes

5. Pulsar Searches

Periodicity Searches: Figure 9 outlines the salient, generic features of periodicity searches. Alternative schemes have been used, including a 2D Fourier analysis of $I(t, \nu)$ rather than dedispersing with trial values of DM. A general discussion can be found in Lyne & Smith (1990).

The single-harmonic threshold, $S_{\min_1}$, is the minimum amplitude that a single FFT component must have to detected:

$$S_{\min_1} = \frac{m S_{\rm sys}}{(n_{pol} \Delta\nu T)^{1/2}}, \tag{26}$$

where m = number of σ corresponding to the detection threshold; $S_{\rm sys} = T_{sys}/G$; T_{sys} = system temperature; G = gain (K Jy^{-1}); $n_{pol} = 2$ if two polarization channels are used in the search; $\Delta\nu$ = total bandwidth; and T = total integration time. Because many statistical tests are performed, $m \sim 8 - 10$.

Harmonic Summing: Survey DFTs are analyzed by constructing partial sums of harmonics (of the DFT magnitude or squared magnitude) for different trial periods. If multiple harmonics are above threshold, then the minimum detectable flux density is

$$S_{\min} = \frac{S_{\min_1}}{h(N_h)}, \tag{27}$$

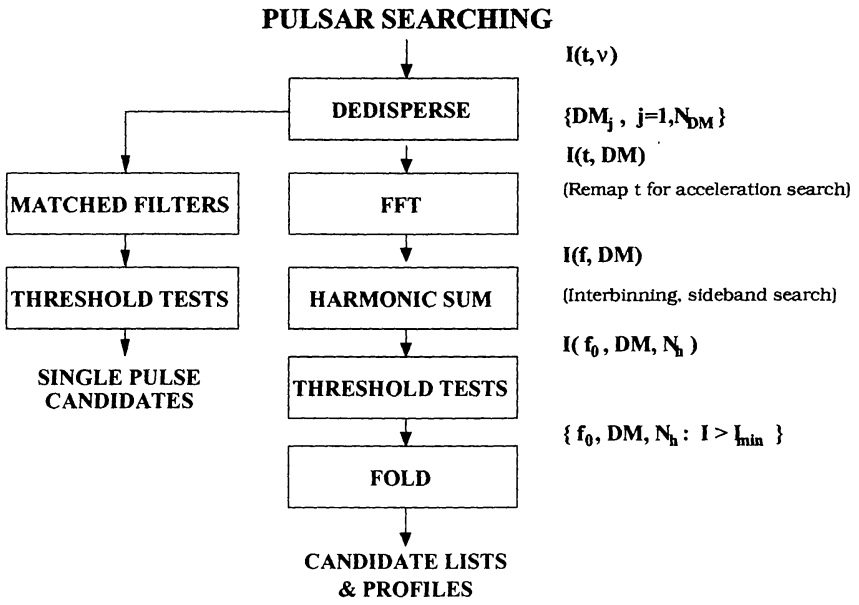

Figure 9. Generic pulsar search analysis including alternative paths for treating pulsars in binaries and for detection of individual pulses with matched filters corresponding to different pulse widths.

$$h(N_h) \;=\; N_h^{-1/2} \sum_{\ell=1}^{N_h} R_\ell, \tag{28}$$

where $h(N_h)$ is the harmonic sum, normalized by $N_h^{-1/2}$ to take into account reduction of the noise in the harmonic sum, which lowers the threshold. For a given data set, the harmonic sum is maximized as a function of N_h. The quantity R_ℓ is related to the Fourier transform of the measured pulse shape. In actual practice, the harmonic sum is calculated up to some maximum N_h and Fourier amplitudes calculated from the DFT are usually interpolated to compensate for discreteness effects.

Distortions of the pulse shape may all be considered in the Fourier domain. These include: dispersion smearing, scattering broadening, rise time of spectrometer filters, postdetection smoothing, and smearing from orbital acceleration. Letting the DFTs of the intrinsic pulse shape, and the time constant, dispersion, scattering and orbital functions be $\tilde{s}_{\rm i}$, $\tilde{s}_{\rm tc}$, $\tilde{s}_{\rm d}$, $\tilde{s}_{\rm s}$ and $\tilde{s}_{\rm orb}$, respectively, we may write the effective envelope function of harmonics, where ℓ = harmonic number, as

$$\tilde{s}_{\rm eff}(\ell) = \tilde{s}_{\rm i}(\ell)\tilde{s}_{\rm tc}(\ell)\tilde{s}_{\rm d}(\ell)\tilde{s}_{\rm s}(\ell)\tilde{s}_{\rm orb}(\ell). \tag{29}$$

The quantity R_ℓ is the ratio

$$R_\ell \equiv \left| \frac{\tilde{s}_{\rm eff}(\ell)}{\tilde{s}_{\rm eff}(0)} \right|. \tag{30}$$

For a pulsar with period-averaged flux density S at distance D, the maximum distance that the pulsar is detectable is

$$\mathrm{D_{max}} = \left(\frac{\mathrm{L_p}\sqrt{N_h}}{S_{\mathrm{min_1}}}\right)^{1/2} = D\left(\frac{S}{S_{\mathrm{min_1}}}\right)^{1/2} N_h^{1/4}, \tag{31}$$

where $\mathrm{L_p} = D^2 S$ is the "pseudo luminosity" and N_h is the number of harmonics that maximizes the harmonic sum in a periodicity search.

Figure 10 shows $\mathrm{D_{max}}$ plotted against $S_{\mathrm{min_1}}$, calculated by using the electron density model of Taylor & Cordes (1993; hereafter TC93) to obtain dispersion and scattering as a function of distance.

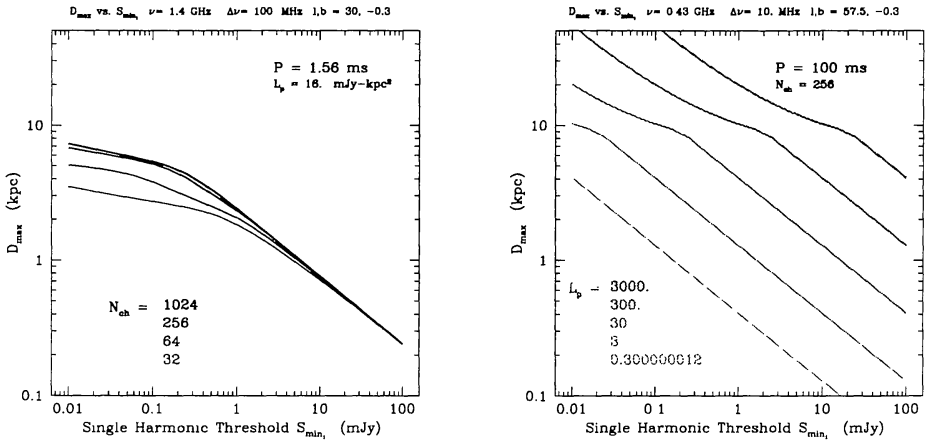

Figure 10. Left: $\mathrm{D_{max}}$ plotted against single harmonic threshold, $S_{\mathrm{min_1}}$, for a 100 MHz bandwidth at 1.4 GHz, a direction $\ell, b = 30°, -0.3°$, P=1.56 ms, and $\mathrm{L_p} = 16$ mJy kpc^2. The different curves correspond to different numbers of spectrometer channels (heaviest line = 1024 channels, lightest line = 32 channels). At high thresholds, $S_{\mathrm{min_1}} \gtrsim 1$ mJy, $\mathrm{D_{max}}$ is *luminosity limited*, i.e. $\mathrm{D_{max}} \propto S_{\mathrm{min_1}}{}^{-1/2}$. For lower thresholds and small numbers of channels, it is *dispersion limited.* For large numbers of channels, dispersion smearing is negligible and $\mathrm{D_{max}}$ becomes *scattering limited* at low thresholds. These curves apply to *postdetection* search systems. For predetection ("coherent") dedispersing systems, the search can still be scattering limited. Right: $\mathrm{D_{max}}$ vs. $S_{\mathrm{min_1}}$ for P=100 ms and a series of pseudoluminosities, as labelled. The curves apply to a 10 MHz bandwidth at 0.43 GHz and a direction $\ell, b = 57.5°, -0.3°$.

In considering how $\mathrm{D_{max}}$ varies with $S_{\mathrm{min_1}}$, we define three regimes:

1. *Luminosity limited:* $\mathrm{D_{max}} \propto S_{\mathrm{min_1}}{}^{-1/2}$, i.e. the inverse square law.
2. *Dispersion limited:* $\mathrm{D_{max}}$ varies more weakly with $S_{\mathrm{min_1}}$ because at greater distances and hence larger DM, the pulse is smeared more, yielding fewer harmonics. In this case, $\mathrm{D_{max}}$ is a sensitive function of the number of spectrometer channels used in the dedispersion process. As N_{ch} increases,

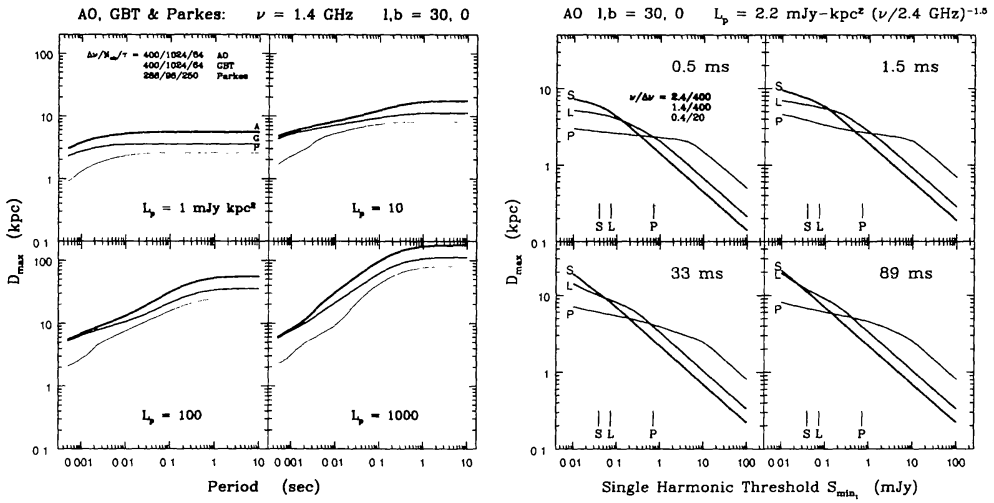

Figure 11. Left: D_{max} vs. P for Arecibo (AO), the Green Bank Telescope (GBT), and Parkes at 1.4 GHz and $\ell, b = 30°, 0°$. For AO and the GBT, spectrometers with 400 MHz total bandwidth, 1024 channels, and 64 μs time resolution are assumed while parameters of the multibeam survey are assumed for Parkes (288 MHz, 96 channels and 250 μs resolution). The four panels are for four different pseudoluminosities. For larger P and L_p, D_{max} extends beyond the nominal disk of the Galaxy. However, high velocity pulsars (e.g. $V > 1000$ km/s) can reach > 30 kpc in their radio emitting lifetimes. Right: D_{max} vs. S_{min_1} for Arecibo at 0.4, 1.4 and 2.4 GHz, labelled as P, L and S, respectively using the scaling $L_p \propto (\nu/2.4\,\mathrm{GHz})^{-1.5}$. The curves indicate that 1.4 GHz is the best of the three frequencies when surveying the Galactic plane.

D_{max} also increases until scattering dominates the pulse broadening. D_{max} is also a strong function of frequency in the dispersion-limited regime.

3. *Scattering limited:* D_{max} varies more weakly with S_{min_1} because scattering broadens the pulse and reduces the number of harmonics. In this case, D_{max} increases quickly with increasing frequency until either the dispersion or the luminosity limited regime is reached.

The *search volume* quantifies a telescope survey's performance:

$$V_s = \frac{1}{3}\Omega_s {D_{max}}^3, \tag{32}$$

where Ω_s is the total solid angle covered and we assume (only for simplicity here) that D_{max} is the same in all directions. Note that some of the search volume can be empty if D_{max} extends past the pulsar population.

Figure 11 shows (left panel) D_{max} plotted against period for Arecibo, the GBT and the Parkes telescope for four luminosities. The same figure also shows (right panel) D_{max} vs. S_{min_1} for Arecibo at three frequencies. Except for short periods and very low thresholds, surveys at L band (1.4 GHz) are superior to

those at S band (2.4 GHz) or P band ($\sim$ 400 MHz). Figure 12 shows contours of $S_{\rm min}$ plotted against P and DM for two surveys: 0.43 GHz using the Arecibo Telescope and 1.4 GHz using the Green Bank Telescope. Scalloping of the contours is caused by gridding in the set of DMs used to dedisperse. However, it should be emphasized that surveys with the GBT toward the Galactic Center will be influenced by much heavier scattering than is included in these figures. Consequently, frequencies as high as 10 GHz may be required to find pulsars in the Galactic Center (Cordes & Lazio 1997).

Guidelines for Optimizing Surveys: By considering the distribution of pulsars in the Galaxy along with the role of propagation effects in searches, a number of basic guidelines emerge:

1. For equal time-bandwidth products, aperture efficiencies, and system temperatures, the larger of two telescopes searches the greatest volume in a single beam.
2. For fixed total survey time, maximizing the number of independent pointings also maximizes the volume surveyed. It is more efficient to increase the volume by adding new pointings rather than increasing the integration time per pointing, which increases $\rm D_{max}$ fairly slowly.
3. When pulses are smeared by distance dependent propagation effects, building a better telescope and backend produces diminishing returns. The total volume surveyed then increases much more strongly with number of pointings (for fixed total time).
4. When searching by tracking a grid of positions, the slewing overhead time determines the optimal integration time per pointing and thus the solid-angle coverage of a survey with fixed total integration time. Note this conclusion holds only if all directions and locations are equally good for discovering objects.
5. When searching the galactic disk, the number of pointings is bounded, thus determining the survey depth as a function of the total survey time.
6. When searching a subpopulation located at some distance from the observer, the integration time is set by the need to reach this distance.
7. It is suboptimal to use telescope time to integrate longer in a given direction than the time it takes to reach a distance such that pulse broadening becomes important. It is better to move to another sky position unless a subpopulation's distance requires a longer integration time.
8. The number of spectrometer channels should be optimized so that pulse broadening from dispersion smearing is smaller than the pulse width for all spin periods of interest.
9. For a disk population with scale height H, it is optimal to (i) choose an integration time per pointing that reaches the edge of the distribution at distance $H/|\sin b|$; and (ii) If the entire volume cannot be searched, then the search should start at $|b| = 90^\circ$ and work downwards in $|b|$.

Effects of Binary Motion: Figure 13 shows how binary motion smears the pulse and diminishes the Fourier amplitudes and harmonic sums. Such effects are

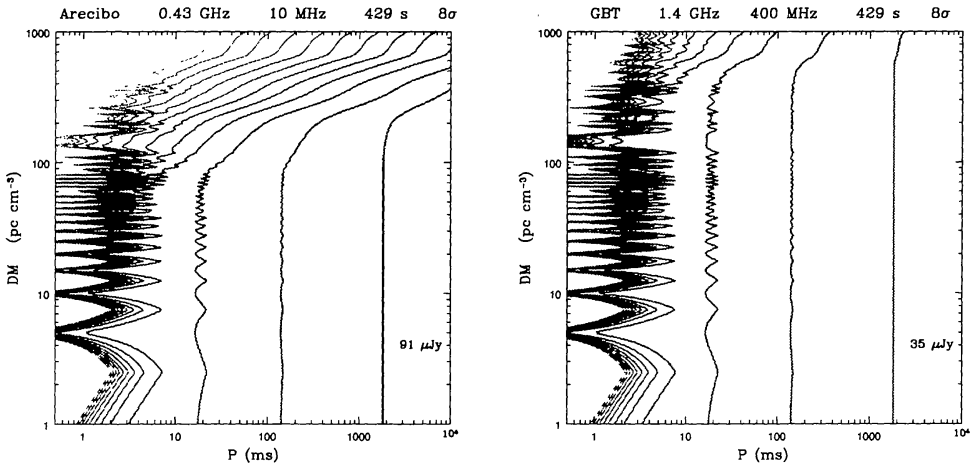

Figure 12. Contours of $S_{\rm min}$ vs. P, DM. The minimum detectable flux density is given on the bottom right of each plot and the contours are at $\times 2^n$ larger values. Contours take into account the change of pulse duty cycle with period ($\propto P^{-1/2}$), dispersion and pulse broadening according to the TC93 model, discreteness of the DM grid used for dedispersion, and harmonic summing up to 32 harmonics. Left: 0.43 GHz and 1024 channels for the Arecibo Telescope. Right: 1.4 GHz and 512 channels for the Green Bank Telesope.

important for integration times as short as a few minutes if the spin period is small and the orbital period is small.

Details about the effects of binary motion on pulsar searches can be found in Johnston & Kulkarni (1991).

Giant Pulse Searches: Giant pulses are defined as those from a distinct component of the pulse amplitude distribution having much larger than average amplitudes. Though only two pulsars are known to show giant pulses — the Crab pulsar (Staelin & Reifenstein 1968) and the millisecond pulsar B1937+21 (Cognard et al. 1996) (Figure 14)— only the Crab pulsar and any of its clones would be found with greater S/N in a search for single dispersed pulses than in a periodicity search. (In fact, the Crab pulsar was first detected in the radio via its giant pulses.) However, because individual giant pulses can be detected quite far away (~0.5 to 1 Mpc for the largest pulse seen in 1 hour) and because young pulsars like the Crab are important to survey, it is always sensible to search for isolated pulses while doing periodicity searches. As shown in Figure 9, an isolated pulse search may be conducted on the same dedispersed time series used in the periodicty searches. The computational cost is minimal.

For a single-pulse search of pulses with width W and amplitude I_m in a bandwidth $\Delta\nu$, we have $(S/N)_{\rm gp} = I_m(n_{\rm pol}\Delta\nu W)^{1/2}/S_{\rm sys}$, where $n_{\rm pol}$ is the number of polarizations summed. This can be compared with a periodicity search over a time $T = N_p P$. With $N_h \approx P/W$ harmonics detected and summed, we have $(S/N)_{\rm hs} = \bar{\rm I} N_p^{1/2}(n_{\rm pol}\Delta\nu W)^{1/2}$, where $\bar{\rm I}$ is the period-averaged intensity $\bar{\rm I} \sim (W/P)\langle I\rangle$ and $\langle I\rangle$ is the mean intensity over the PDF of *peak* pulse

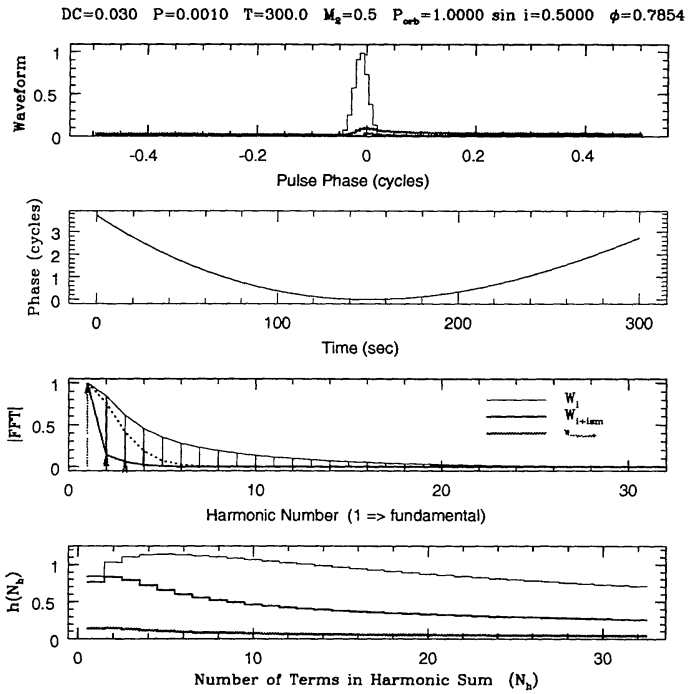

Figure 13. Pulse smearing by binary motion results in attenuation of harmonics and the harmonic sum. Shown is a case for a pulsar with P = 1 ms and an intrinsic duty cycle of 3%. The orbital period is 1 hr and the companion mass is 0.5 $M_\odot$. From top to bottom the panels are: 1. Intrinsic pulse shape (tallest), smeared pulse shape (next tallest) and smeared delta function. 2. Spin phase perturbation from orbital motion. 3. FFT magnitude for the intrinsic pulse shape (light line), pulse smeared by interstellar effects (dashed line), and pulse smeared by orbital and interstellar effects (heavy line). 4. Harmonic sum vs. number of terms in sum for intrinsic, ism-smeared, and ism+orbitally smeared. The harmonic sum maximizes at progressively smaller N_h as the smearing increases.

intensities. To compare the two kinds of seaches, we consider a simple bimodal distribution

$$f_I(I) = (1-g)\delta(I-I_1) + g\delta(I-I_2), \qquad 0 \le g \le 1, \tag{33}$$

where g is the probability of giant pulses with amplitudes I_2. We must have at least one giant pulse in a given interval of N_p pulse periods, requiring on average $g \ge g_{\rm min} \sim N_p^{-1}$. To have $S/N_{\rm gp} > S/N_{\rm hs}$, we require

$$g < g_{\rm max} \approx \left[N_p^{-1/2} - I_1/I_2\right] / \left(1 - I_1/I_2\right). \tag{34}$$

Figure 15 shows the domains of g and I_1/I_2 for which a giant pulse search is the superior method. The results depend on N_p in that larger N_p yield smaller domains.

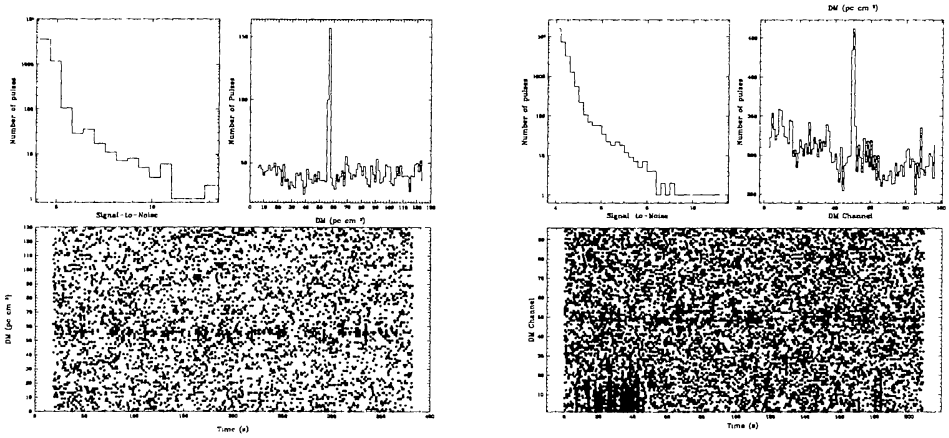

Figure 14. Single pulses from two pulsars. Left: Crab pulsar (P = 33 ms, DM = 56.8 pc cm^{-3}). Right: B1937+21 (P = 1.56 ms, DM = 71.04 pc cm^{-3}). For each pulsar, the top left panel is a histogram of signal to noise ratio, the right panel a histogram of candidate DMs, and the lower panel shows events plotted against time and DM channel. For B1937+21, radio frequency interference causes the events at low DMs. (Figures courtesy Maura McLaughlin).

Lundgren et al. (1995) inferred a bimodal distribution for the Crab pulsar with a ratio of typical giant pulse (in one hour) to mean pulse amplitude in the weaker component $\sim 10^{-3}$ and with a probability $\sim 10^{-4.4}$. The Crab pulsar has a power-law giant-pulse PDF, however.

6. Arrival-time Precision

Pulsar timing is discussed in the lecture by I. Stairs. Here we summarize briefly how some of the effects discussed in this paper affect the measurement of arrival times. These include

1. **radiometer noise:** contributes a Time of Arrival (TOA) error

$$\sigma_n \approx \left[\frac{21.9\mu\, s}{(S/N)_1}\right]\left(\frac{\theta_{\rm FWHM}}{1\ ms}\right)\left(\frac{\Delta}{\theta_{\rm FWHM}N_3}\right)^{1/2}, \qquad (35)$$

   where Δ is the temporal resolution ($\sim$receiver time constant) and $(S/N)_1$ is the signal-to-noise ratio of a single pulse.
2. **pulse phase jitter:** like that seen in Figure 16 yields a TOA error

$$\sigma_J \approx 13.4\mu s\, f\, (1+m_I^2)^{1/2} N_3^{-1/2}\left(\frac{\theta_{\rm FWHM}}{1\ ms}\right), \qquad (36)$$

   where $\theta_{\rm FWHM}$ is the pulse width (full width at half maximum); $f \approx 1$ is the amount of jitter in units of the observed pulse width; $m_I \approx 1$ is the intensity modulation index (rms/mean); and $N_3 \equiv N/10^3$.

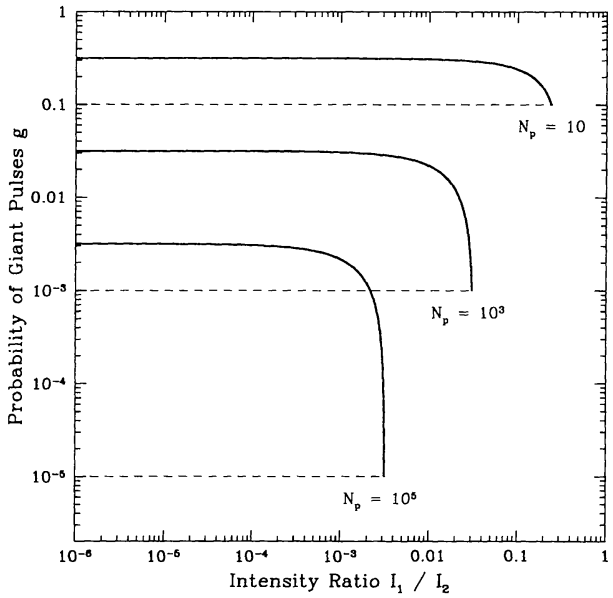

Figure 15. Domain for which a giant pulse search is more sensitive than a periodicity search. The pulse amplitude distribution is assumed to be bimodal. I_1 is the amplitude of ordinary pulses with probability $1-g$ and I_2 is the giant-pulse amplitude with probability g. The results depend on how many pulse periods, N_p, are analyzed. For each of the three cases shown, a giant pulse search is superior for values of g and I_1/I_2 between the dashed and solid lines.

An important conclusion follows from Eqs. 35-36: If $S/N_1 \gtrsim 1$, then the TOAs will be jitter dominated rather than noise dominated. When this is the case, the TOA error can be reduced only by integrating more pulses, not by building a better telescope!

3. **diffractive interstellar scintillation:** The finite number of bright patches in the frequency-time plane yield a $\sqrt{N}$ type error.
4. **pulse broadening:** produces a frequency-dependent and sometimes time-dependent error.
5. **variations in DM and angle-of-arrival from refraction:** DM variations occur because of the electron density variations (e.g. Phillips & Wolszczan (1992).
6. **instrumental polarization:** Total intensity profiles of pulsars are very stable (apart from cases where precession is seen). But pulsars can be highly linearly and circularly polarized. With imperfect calibration, a TOA error is induced on the order of the error in the Stokes parameter I.

7. Pulsar Distances

Table 2 summarizes types of distances estimates and approximate numbers. By far, most distances are estimated using DM and a model for the Galactic distri-

Table 2. Pulsar Distance Estimates

Type	Number	Comments
Parallax		
Interferometry	9	1 mas @ 1kpc, ionosphere
Timing	5	1.6 μs @ 1kpc, timing noise
Optical	1	HST point-spread function
Associations		
Supernova Remnants	8	ISM perturbations
Globular Clusters	16 clusters	Spectroscopic distances
LMC/SMC	8	
HI Absorption	74	bright pulsars, galactic rotation model
DM + Electron Density Model	all radio pulsars	ISM perturbations

bution of free electrons. The model by TC93 is currently being revised (Cordes & Lazio, in preparation). The new model (see Figure 17) consists of several components (thin and thick disks, spiral arms, Galactic Center, and individual regions) that are fitted for and calibrated by the independent measurements summarized in Table 2. The new model, like TC93, yields $n_e(\mathbf{x})$ and $C_n^2(\mathbf{x})$. It can be used with known pulsars by integrating n_e until DM is reached, thus yielding a distance estimate and an estimate for the scattering measure, SM. It can also be used in simulation studies where a pulsar distance is generated by Monte Carlo and then DM and SM are determined.

The new model differs from TC93 by including:

1. doubling of the number of lines of sight with DM and SM measurements;
2. redefinition of the spiral-arms.
3. improved treatment of the local ISM;
4. improved treatment of the outer Galaxy;
5. treatment of the Galactic Center region; and
6. improved fitting analysis using a likelihood function;

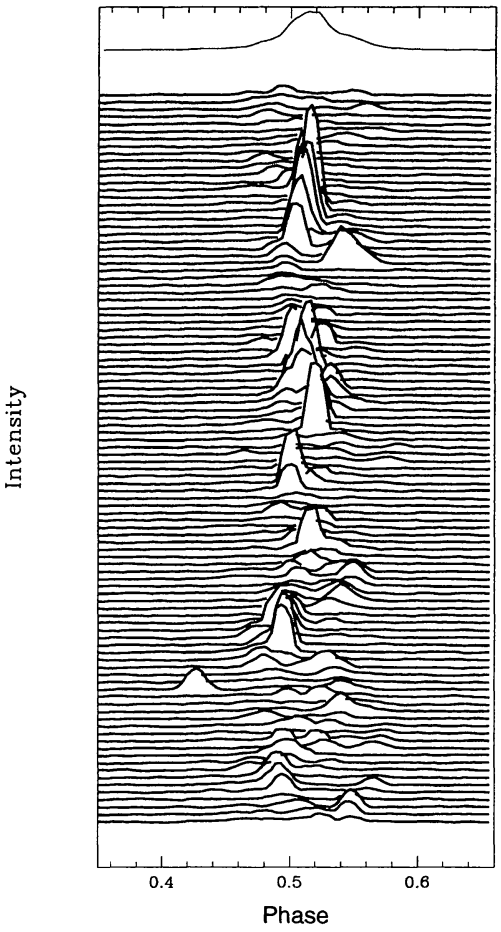

Figure 16. A sequence of pulses from the recently discovered pulsar J1740+1000 (McLaughlin et al. 2002).

8. VLBI Astrometry: If you want a good distance, measure a parallax!

Though the DM + electron-density model method for estimating distances is quite useful, it is also true that the model will never be good enough to estimate distances to all pulsars with reasonable precision (e.g. $\lesssim$10%).

Fortunately, the prospects for measuring parallaxes with VLBI are quite good, even for pulsars as far as 5 kpc or more if they are bright enough. Recent work (Brisken et al. 2000; Chatterjee et al. 2001) has demonstrated methods for removing deleterious ionospheric effects that plague astrometry efforts at cm wavelengths. A combination of self-calibration and usage of extragalactic background calibrators is needed, as discussed in these references. A crucial aspect of pulsar VLBI is *gating* of the correlator (e.g. Gwinn et al. 1986) so that only flux in a narrow window (appropriately shifted according to the DM

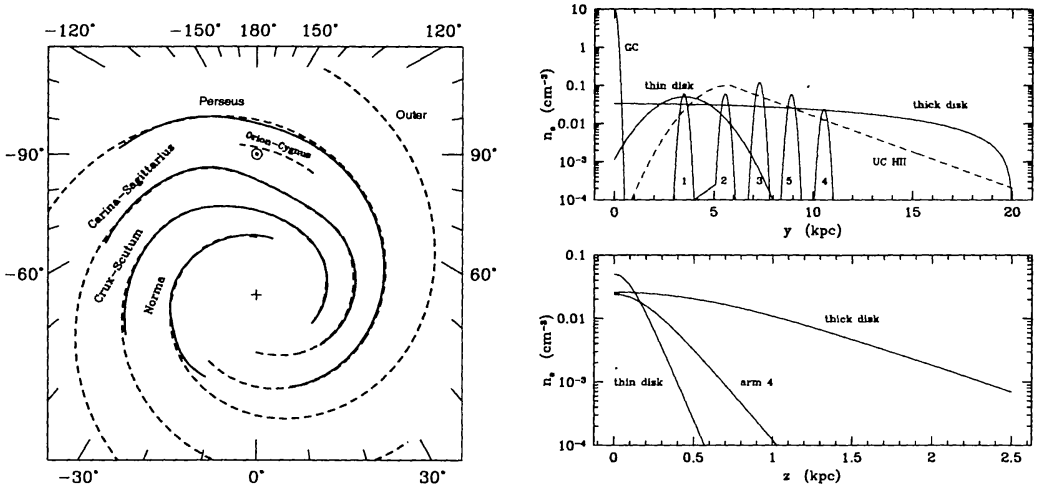

Figure 17. Features of the revised electron density model (Cordes & Lazio, in preparation). Left: Solid lines show the spiral arm definitions used in TC93 while dashed lines show the new spiral arms. The new arms are based largely on a 4-arm logarithmic spiral and yield a better fit. Right: Cross sections of the electron density model. The top panel shows n_e vs. y = coordinate with origin at the Galactic Center and increasing toward the Sun. The bottom panel shows $n_e(|z|)$ for different cuts at different Galactocentric radii (r = 3.5 kpc for the thin disk slice, $r = \mathrm{R}_\odot$ for the thick disk, and the 'arm 4' cut is through the Perseus arm).

delay across the entire band) centered on the pulsar pulse is included. The boost in S/N is $\sim$(duty cycle)$^{-1/2} \sim 3$ to 5 for typical duty cycles of the *window*.

A powerful combination will result when Arecibo, the GBT and the phased VLA are included with the VLBA antennas and EVN antennas. With such an array, pulsars with flux densities less than 1 mJy can be reached in measuring parallaxes as well as proper motions. The large collecting areas on some of the baselines will also allow observations to be conducted at 5 or 8 GHz, frequencies where the ionosphere's effects are much smaller.

9. Pulsar Survey Examples

Galactic Plane Surveys: The Parkes Multibeam (PMB) survey (Camilo et al. 2000) has been extraordinarily successful in discovering new pulsars at 1.5 GHz, owing to the greater $\mathrm{D_{max}}$ afforded by the lessening of propagation effects. Results presented above confirm that 1.5 GHz is the best among 0.4, 1.5 and 2.4 GHz for searching the furthest. Arecibo can search ~ 480 deg^2 of the Galactic plane with $|b| \leq 5°$. Scaling from the PMB survey by solid angle only, we estimate that 240 pulsars could be discovered. However, Arecibo can search to significantly greater $\mathrm{D_{max}}$ and thus greater volume. For $\mathrm{L_p} \lesssim 10$ mJy kpc^2, Arecibo can 'see' about 2.2 times further than Parkes for $P \gtrsim 10$ ms, corresponding to $\times 10$ volume. For millisecond pulsars (MSPs), Arecibo can see factors of 3 to 5 further than the PMB

survey, owing to the anticipated narrower channel bandwidths and shorter dump times of Arecibo spectrometers. About 1000 pulsars could be found using Arecibo in a 7-beam multibeam survey, requiring a total bandwidth of 300 MHz with 1024 channels and 3000 hr of telescope time divided into 300-500 s per beam. The GBT can search a much larger solid angle in the Galactic plane though with less sensitivity than Arecibo. Nonetheless, the GBT will be a powerful instrument for discovering large samples and exotic pulsars.

High Latitude Searches for MSPs, NS-NS and NS-BH Binaries, and High-velocity Pulsars. Looking out of the Galactic plane, propagation effects are smaller and it is advantageous to search at lower frequencies in order to exploit the larger pulsed flux. MSPs have a scale height $H \sim 0.5$ kpc, so out of plane searches can be designed that search out to $H/|\sin b|$. The greatest volume available to be searched is at small $|b|$, where propagation effects are greatest. Thus the optimal latitude is roughly 10 to 20 deg. NS-NS binaries have sufficiently large space velocities that their scale height is expected to be about 5 kpc. This also favors a high-latitude search. NS-BH binaries also should have a sizable scale height though not as great as NS-NS binaries, since the BH formation process may not yield a kick and also because such binaries are more massive than NS-NS binaries. Isolated pulsars with high space velocities extend to very large $|z|$. About 50% of all NS will escape the Galaxy (Arzoumanian, Chernoff, & Cordes 2002, submitted; Lyne & Lorimer 1994) and can reach $> 10^3$ km s^{-1} $\times$ 10 Myr = 10 kpc in their typical radio-emitting lifetimes. A deep, low frequency search is clearly appropriate for discovering members of this population.

The Galactic Center(GC): The star cluster may contain as many as 10^7 NS; most will be radio quiet though there are probably many MSPs in the star cluster. A star burst within the last 10 Myr may have produced a significant population of active radio pulsars. Pulse broadening is notoriously large for pulsars near Sgr A*: $\tau_d \sim 300$ s at 1 GHz (Cordes & Lazio 1997). Exploiting the strong frequency dependence ($\tau_d \propto \nu^{-4}$), a search at 10 GHz is suggested. Some known pulsars placed at the GC are detectable at this frequency. Payoff includes study, through pulse timing, of the ISM in the GC and the gravitational potential in the star cluster and, possibly, near Sgr A*.

Extragalactic Giant Pulses: The Crab pulsar sporadically emits large amplitude ("giant") pulses that are hundreds to thousands of times the mean pulse amplitude (Hankins & Rickett 1975; Lundgren et al. 1995). The pulse amplitude distribution is a power law such that, at 0.4 GHz, the largest pulse seen at roughly one-hour intervals is visible to ~ 1 Mpc using an Arecibo-sized telescope. The giant-pulse phenomenon is poorly understood but it may be associated with pulsars having small light cylinders, i.e. young pulsars and MSPs. Searches for giant pulses from pulsars in nearby galaxies may be made either through blind searches or through targetting of known supernova remnants in those galaxies. The payoff is greatest if an ensemble of pulsars can be found in a given galaxy so that

the contributions of the intergalactic medium and the ISMs of the Galaxy and the host galaxy can be disentangled.

References

Armstrong, J. W., Rickett, B. J., & Spangler, S. R. 1995, ApJ, 443, 209

Arzoumanian, Z., Chernoff, D. F., & Cordes, J. M. 2002, ApJ, 568, 289

Brisken, W. F., Benson, J. M., Beasley, A. J., Fomalont, E. B., Goss, W. M., & Thorsett, S. E. 2000, ApJ, 541, 959

Camilo, F. et al. 2000, in ASP Conf. Ser. Vol. 202, in IAU Colloq. 177, Pulsar Astronomy – 2000 and Beyond, ed. M. Kramer, N. Wex & R. Wielebinski (San Francisco: ASP), 3

Chatterjee, S., Cordes, J. M., Lazio, T. J. W., Goss, W. M., Fomalont, E. B., & Benson, J. M. 2001, ApJ, 550, 287

Cognard, I., Shrauner, J. A., Taylor, J. H., & Thorsett, S. E. 1996, A&A, 323, 211

Cordes, J. M. & Lazio, T. J. W. 1991, ApJ, 376,123

Cordes, J. M. & Lazio, T. J. W. 1997, ApJ, 475, 557

Cordes, J. M. & Rickett, B. J. 1998, ApJ, 507, 846

Cordes, J. M., Weisberg, J. M., Frail, D. A., Spangler, S. R., & Ryan, M. 1991, Nature, 354, 121

Gwinn, C. R., Taylor, J. H., Weisberg, J. M., & Rawley, L. A. 1986, AJ, 91, 338

Hankins, T. H. & Rickett, B. J. 1975, in Methods in Computational Physics Volume 14 – Radio astronomy (New York: Academic Press), 55

Johnston, H. M. & Kulkarni, S. R. 1991, ApJ, 368, 504

Lundgren, S. C., Cordes, J.M., Ulmer, M., Matz, S., Lomatch, S., Foster, R. S., & Hankins, T. H. 1995, ApJ, 453, 433

Lyne, A. G. & Smith, F. G. 1990, Pulsar Astronomy (Cambridge: Cambridge University Press)

Lyne, A. G. & Lorimer, D. R. 1994, Nature, 369, 127

McLaughlin, M., Arzoumanian, Z., Cordes, J. M., Backer, D. C., Lommen, A. N., Lorimer, D. R., & Zepka, A. F. 2002, ApJ, 564, 333

Phillips, J. A. & Wolszczan, A. 1992, ApJ, 385, 273

Rickett, B. J. 1990, ARA&A, 28, 561

Staelin, D. H. & Reifenstein, E. C. III 1968, Science, 162, 1481

Taylor, J. H. & Cordes, J. M. 1993, ApJ, 411, 674

Thomson, R., Moran, J., & Swenson, G. W. 2001, Interferometry and Synthesis in Radio Astronomy, (2nd edition; New York: Wiley-Interscience)